Virtual Laboratory Environment for High Voltage Radiation Source Experiments

Calabazas Creek Research, Inc.
&
University of California at Berkeley

Contract Number FA9550-04-C-0069

Item Number 0001AA

Final Report

Introduction

The overall technical objective of the Phase I work was to demonstrate the feasibility of a computational virtual laboratory for simulating high voltage effects, herein called VLAB. Models in support of this objective were identified and defined in Phase I, with some components implemented in the one-dimensional object oriented code, OOPD1, and others implemented directly in the 2D code XOOPIC. OOPD1 serves as a training vehicle for new students and a platform for rapid prototyping of new algorithms. The simplicity of OOPD1 ensures that the algorithm or model remains the focus, rather than the mathematical and programming details of multi-dimensional implementation. In Phase II, all final implementation will be in the two-dimensional VLAB code, based on the well-tested XOOPIC particle-in-cell code.

The results of Phase I of this work are summarized in this section. In Task 1, the work related to modeling the formation of a moving plasma cathode interface is described. The Task 2 work related to scattering of energetic electrons is discussed. Work related to high voltage breakdown of insulator surfaces is discussed in Task 3. Models for intense heat fluxes to surfaces is described in Task 4, and models for generation of x-rays are discussed in Task 5. Work related to detailed structural visualization of high voltage microwave devices is discussed in Task 6.

Task 1: Moving Plasma Cathode

Plasma formation near electrode surfaces can result when desorbed impurities or sputtered neutrals are ionized by energetic electrons or x-rays. Even in the presence of strong fields, the space charge of the plasma can lead to formation of a virtual cathode. Temporal variations in the fields

or plasma density can lead to translation of the point at which the field is zero, leading to the analogy of a moving Child-Langmuir space charge limited emitter in the presence of fields that extract electrons from the plasma.

A suite of models was developed for emission from a moving plasma cathode surface during Phase I of the research. The following models are required for study of emission from plasma cathodes. An effective field enhancement model was developed to incorporate geometric surface effects at the sub-grid level, as well as to include geometric field enhancement in models with lower spatial dimensionality. The transition from Fowler-Nordheim field emission current to space-charge limited current was also described. We also investigated hybrid models for representing more dense plasmas, which may be formed near emitting surfaces, particularly particle-fluid hybrids capable of retaining important kinetic effects. The standard Monte Carlo collision model was extended to the relativistic regime. Sputtering and desorption models for particle impact at surfaces were also described.

Geometric Field Enhancement of Emission

A field enhancement factor is often required at the macroscopic scale in order to explain field emission current densities due to geometric features. The local field enhancement factor β is often introduced in the Fowler-Nordheim equation to represent the geometrical effects at the surface of the cathode, where $\beta(s) = E(s)/E_o$. Local variation of β determines the local surface electric field, resulting in local dependence of injection current by the Fowler-Nordheim law. In computational models, it is impractical to determine the time-dependent local surface field for each time step on a microscopic space scale. Effective β is introduced in order to facilitate study of the emission properties at a macroscopic scale. Microscopic (subgrid) local β is calculated only at the initial time step, and then the effective enhancement, β_{eff}, can be recomputed under different surface electrical fields through this model. The model allows reduction of dimensionality as well as the ability to include subgrid effects. The model is demonstrated on fundamental cases and compared to a calculation with a mesh fine enough to resolve the geometric features.

The basic field emission effect involves reduction of the tunneling barrier for electrons within a surface, described by the well-known Fowler-Nordheim equation, modified here to include the local field enhancement factor [1]:

$$J_{FN}(s) = \frac{A(\beta(s)E_o(s))^2}{\phi_w t^2(y)} \exp\left(\frac{-B\nu(y)\phi_w^{3/2}}{\beta(s)E_o(s)}\right) \text{A/m}^2 \qquad \text{(EQ 1)}$$

where $E(s)$ is the normal component of electric field at a 1D, 2D, or 3D surface s, ϕ_w is the work function of the metal, A and B are empirical constants, $y = 3.79 \times 10^{-5}(\beta(s)E_o(s))^{1/2}$, and $\beta(s) = E(s)/E_o(s)$ is the ratio of the local surface electric field to the applied field. $\upsilon(y)$=0.95-y2 and $t(y) \approx 1.1$ are functions that arise due to the inclusion of image charge effects. It has been noted that this field enhancement may come not only from geometric effects but also from impurities [2,3].

The methodology for incorporating β_{eff} is described by the following. Starting from the surface geometry, the local electric fields due to an applied field are solved at t=0 to obtain the local field

enhancement β at each point along the surface. Next, the effective current for a given applied field is found and then β_{eff} is determined over the emitting surface.

Effective field enhancement β_{eff} is defined for most the general case by integrating the current over the emitting surface numerically,

$$J_{ave\_FN} = \frac{1}{A_s}\int_S J_{FN}\, ds = \frac{1}{A_s}\int_S \frac{A(\beta(s)E_o(s))^2}{\phi_w t^2(y)} \exp\left(\frac{-Bv(y)\phi_w^{3/2}}{\beta(s)E_o(s)}\right) ds \quad \text{(EQ 2)}$$

$$= \frac{1}{A_s}\int_S \frac{A(\beta_{eff}(s)E_o(s))^2}{\phi_w t^2(y)} \exp\left(\frac{-Bv(y)\phi_w^{3/2}}{\beta_{eff}(s)E_o(s)}\right) ds \quad \text{(EQ 3)}$$

where A_S is the emitting surface area. In our implementation, we subdivide the cathode with many small intervals and use Simpson's 3/8 rule to integrate (2) in each interval, then use the bisection method to invert (3) for β_{eff}. For the case that $E_o(s)$ is a constant over the surface of cathode, we can simply set

$$J_{ave\_FN} = \frac{A(\beta_{eff}(s)E_o)^2}{\phi_w t^2(y)} \exp\left(\frac{-Bv(y)\phi_w^{3/2}}{\beta_{eff}(s)E_o}\right) \quad \text{(EQ 4)}$$

Without the consideration of A_E, the effective β will include all the information for the surface of the cathode. This can be applied to reduce the dimensionality required to model higher dimension geometry, as well as allow for gridding which does not resolve the underlying geometry. The process is illustrated by example in Fig. 1 for an analytic local field enhancement factor.

Fowler-Nordheim Transition to Space Charge Limited Emission

The Fowler-Nordheim law gives the current density extracted from a surface under strong fields by treating the emission of electrons from a metal-vacuum interface in the presence of an electric field normal to the surface as a quantum mechanical tunneling process. Child's law predicts the maximum transmitted current density by considering the space charge effect. At low fields, the transmitted current is limited by Fowler-Nordheim's law, and at high fields it is limited by Child's law. This work analyzes the transition of the transmitted current density from the Fowler-Nordheim law to the Child's law space charge limit using the one-dimensional OOPD1 code. Also studied is the response of the OOPD1 emission model to strong electric fields near the transition point. Methods for increasing the current density to approach the space charge limit by modifying the device design are also described.

In Fig. 2, the Fowler-Nordheim current is compared to the space charge limited current for β=1 and β=10 in a fixed 10^{-6} m gap for varying applied field. Here applied field is defined as the applied gap voltage divided by the gap width. In this model, the β is held fixed, when in fact it should appear as β_{eff} and vary with the applied field according to the preceding section. Note that in these coordinates, the space charge limiting current is independent of β, and depends only on the applied field (with gap held fixed, and holding emission velocity fixed and small compared to the applied voltage). From these results, it requires $\beta \geq 10$ to approach the space charge limited

(a)

Beta Enhancement Factor

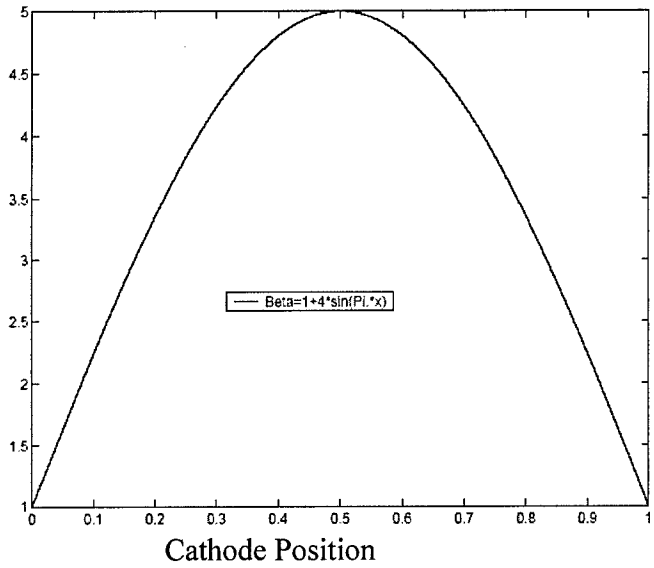

(b)

Emitted Current Density

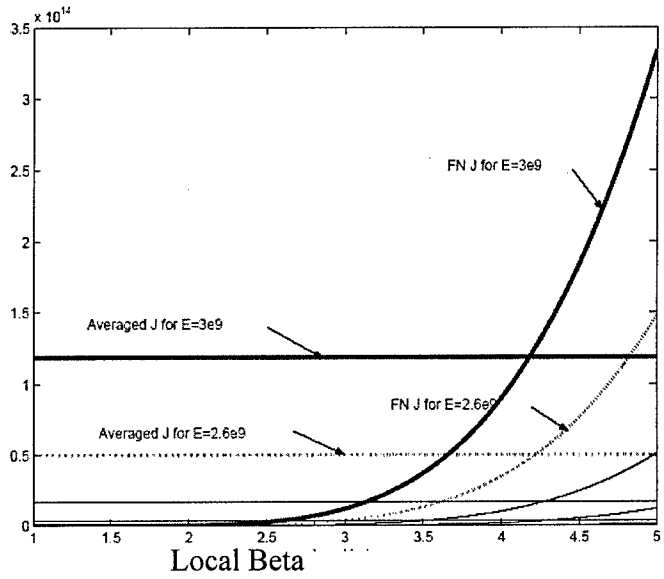

(c)

Effective Beta

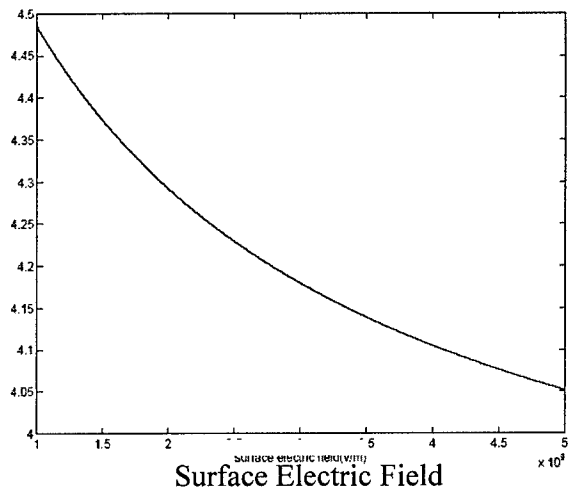

Figure 1. Example of effective beta: (a) local dependence of β, (b) averaged Fowler-Nordheim current density, and (c) fitted line between β_{eff} and surface electric field

current, as the space charge otherwise suppresses the surface field, and neither the Fowler-Nordheim current nor the space charge limited current can be reached even at high applied field strength.

Hybrid Models

One significant computational limitation of modeling the formation of a plasma cathode is that the densities can become significant, making a particle approach computationally intensive. However, in order to capture non-equilibrium and kinetic behaviors, a particle method is preferred. In order to make PIC codes more efficient for high density distributions, which contain a significant thermal part of the distribution, a hybrid particle-fluid model is considered. In Phase I, a number of candidate methods were identified, as discussed below.

Fluid behavior is determined by the Navier-Stokes equations:

$$\frac{\partial n}{\partial t} + \nabla \cdot (n\mathbf{v}) = 0 \qquad \text{(EQ 5)}$$

$$mn\left(\frac{\partial \mathbf{v}}{\partial t} + (\mathbf{v} \cdot \nabla)\mathbf{v}\right) = qne(\mathbf{E} + \mathbf{v} \times \mathrm{B}) - mn\mathbf{v}\nu_m - \nabla p \qquad \text{(EQ 6)}$$

$$\frac{\partial}{\partial t}\left(\frac{3}{2}p\right) + \nabla \cdot \frac{3}{2}(p\mathbf{v}) + p\nabla \cdot \mathbf{v} + \nabla \cdot \mathrm{Q} = \left.\frac{\partial}{\partial t}\left(\frac{3}{2}p\right)\right|_c \qquad \text{(EQ 7)}$$

Relativistic forms may be used if necessary.

The ideal gas equation is used as an equation of state:

$$p = nT \qquad \text{(EQ 8)}$$

The temperature, T, is in eV.

First, consider electrostatic hybrid models. One simple model, often called a Boltzmann-PIC hybrid [4], represents part of the electron distribution with inertialess fluid electrons obeying Boltzmann's relation. Neglecting the left side of Eq. (6), and assuming driftless species with pressure balancing the electric field for the isothermal case,

$$0 = nq\nabla\Phi + \nabla(neT) \qquad \text{(EQ 9)}$$

$$n(\mathbf{x}) = n_o \exp(-q\Phi(\mathbf{x})/\mathrm{T}) \qquad \text{(EQ 10)}$$

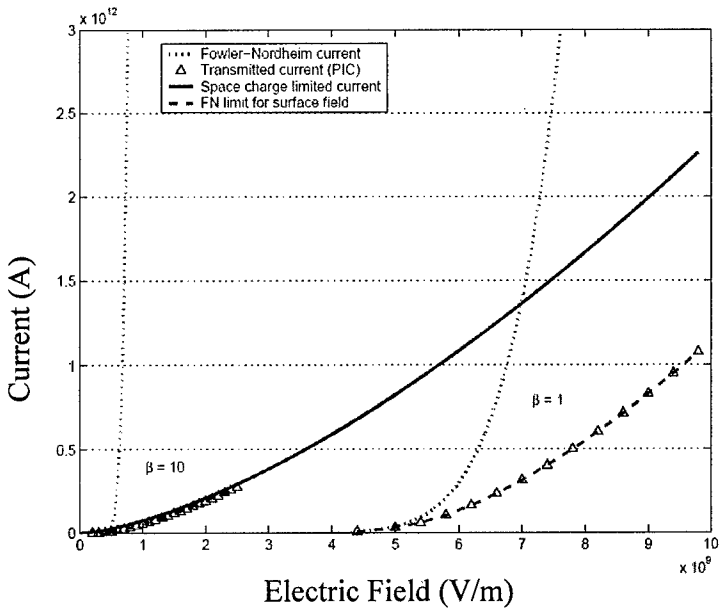

Figure 2. Transition from Fowler-Nordheim to space charge limited current for a fixed gap of 10^{-6} m, for $\beta = 1$ and $\beta = 10$.

n_0 is the density where $\Phi = 0$. Poisson's equation becomes a nonlinear expression for Φ. For a single Boltzmann species:

$$\nabla^2\Phi = -\frac{1}{\varepsilon_o}[\rho_{ext}(\mathbf{x}) + qen_o \exp(-q\Phi(\mathbf{x})/\mathrm{T})] \quad \text{(EQ 11)}$$

$\rho_{ext}(\mathbf{x})$ is the charge density at $\mathbf{x}$ from all sources other than the Boltzmann species. Eq. (11) may be solved with a nonlinear numerical solver.

The next level of complexity of the fluid model is the drift-diffusion approximation. The drift-diffusion approximation also includes the same two right-hand side terms from the momentum equation (Eq. (6)) as the Boltzmann approximation and also includes the collisional term, $mn\mathbf{v}\nu_m$:

$$\mathbf{v} = \frac{q\mathbf{E}}{m\nu_m} - \frac{eT}{m\nu_m}\frac{\nabla n}{n} \quad \text{(EQ 12)}$$

This assumes ν_m is known or may be calculated. Assuming T is known, there are now two variables (n,$\mathbf{v}$), as opposed to one for the Boltzmann approximation. The system may be closed by using the continuity equation (Eq. (5)). The charge density is added to the Poisson equation, as in the Boltzmann approximation.

Sommerer and Kushner [5] simulate RF discharges, including chemical reactions in gas mixtures (He, N_2, O_2, CF_4, SiH_4, NH_3) using a 1D hybrid model consisting of a Poisson solver and drift-diffusion fluid model (including chemistry terms), an electron Monte Carlo simulation, and a neutral chemistry and transport model. Ion mobilities are from tabulated values and electron mobilities are generated as a curve fit to the collision frequencies calculated from the previous Monte Carlo iteration. The diffusion coefficient is determined using the Einstein relation, $D = \mu kT$. Averaging is done over several RF cycles, keeping the phase of the dependent variables, and the electron Monte Carlo model, the fluid model, and the chemistry model are iterated over until the system converges to an oscillatory system. Results are compared with experimental data.

Since Coulomb collisions are important for high density plasmas, it is problematic that the standard PIC method under-represents the Coulomb force for particles within a cell, as shown in Fig. 3. A new technique developed partially under Phase I of this program is the treecode method [6], in which particles interact directly via Coulomb's law at short range, but interact as clusters of particles at long range.

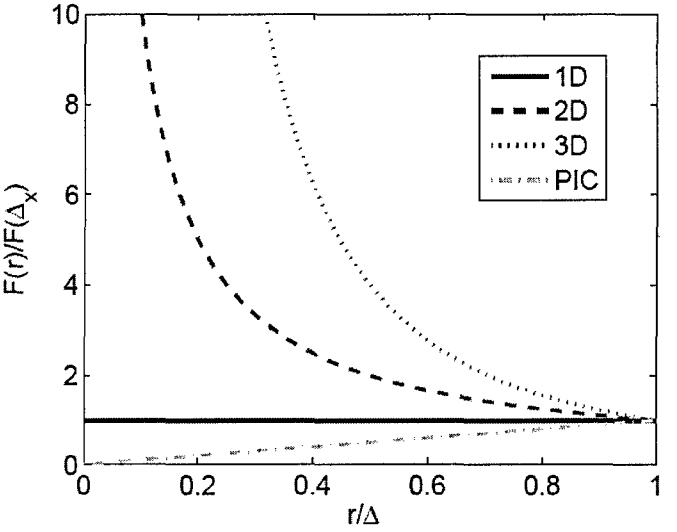

Figure 3. Force between two PIC particles separated by a distance r using linear weighting, compared to Coulomb's law in 1D, 2D, and 3D

The homogenous solution is obtained via a boundary integral method. This allows the method to include both the short and long range Coulomb collision operators, while still resulting in an $N \log N$ method for N particles, comparable to the PIC scheme. Because the method is gridless, it offers an efficient scheme for modeling non-conformal boundaries. The method requires spatial sorting of particles. Many details have not yet been resolved for the treecode method, such as the consequence for noise properties resulting from the short range Coulomb interaction.

A comparison of the treecode scheme with the classical PIC model is shown in Fig. 4 for a one-dimensional virtual cathode oscillation. Note that the PIC method results in a sharper oscillation, because the short range Coulomb collisions in the treecode result in lower peak densities and consequently a weaker interaction at the peak. The higher peak densities at the turning point in the PIC code result in exaggeration of the current modulation, which can be seen as gaps in the velocity-position phase space. A direct application of Coulomb's law agrees well with the treecode result, while the PIC result converges to the treecode result for $\Delta x \rightarrow 0$.

Next, we consider electromagnetic models. The drift-diffusion approximation may also be formulated with the assumption of a magnetic field for electromagnetic plasmas. In this case, there are two diffusion and mobility terms – those along field lines and those across field lines. The quantities along the magnetic field are the same as the electrostatic case. As with the electrostatic case, the momentum collision frequency must be known or calculable.

The mobility and diffusion coefficients for crossing magnetic field lines are related to electrostatic quantities [7]:

$$\mu_{\perp} = \frac{\mu}{1 + (\omega_c / \nu_m)} \qquad \text{(EQ 13)}$$

$$D_{\perp} = \frac{D}{1 + (\omega_c / \nu_m)} \qquad \text{(EQ 14)}$$

ω_c is the cyclotron frequency.

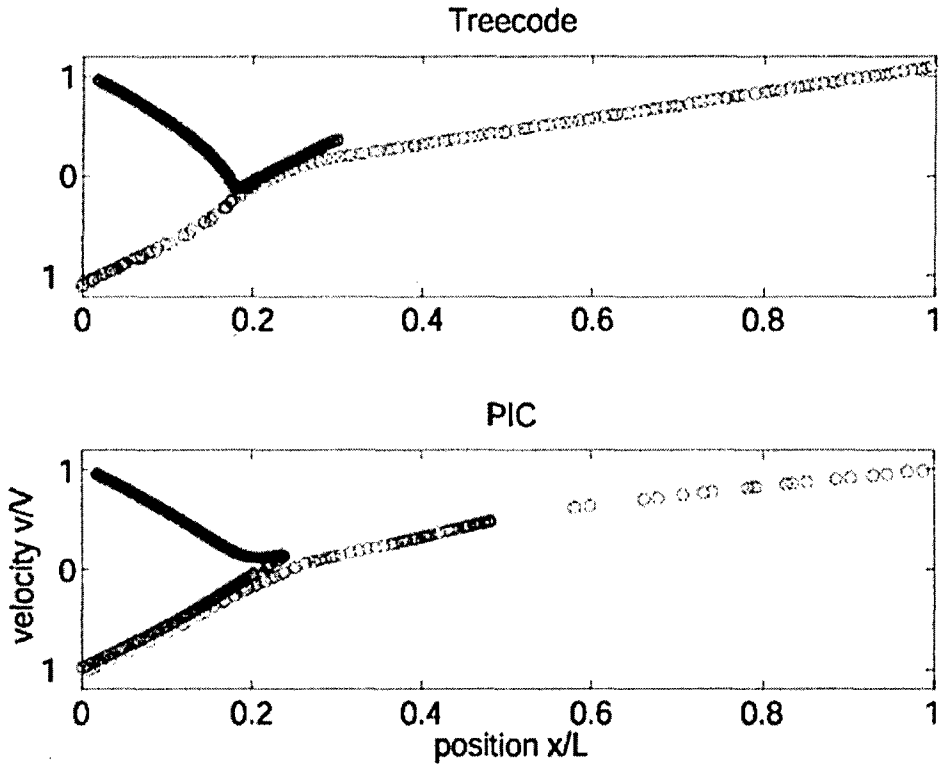

Figure 4. Comparison of treecode (top) and PIC (bottom) models for a one-dimensional virtual cathode oscillation.

Omelchenko [8] develops a 3d-hybrid PIC code using the assumptions of quasineutrality and neglecting displacement current. The electrons are modeled as a massless fluid collisionally coupled with ions and neutrals. The ions are advanced as PIC particles with additional drag terms for collision frequencies.

$$\nabla \times \mathbf{B} = \mu \mathbf{J} \tag{EQ 15}$$

$$\mathbf{E} = \eta_e \mathbf{J}_e + \eta_i \mathbf{J}_i + \frac{\mathbf{J}_e \times \mathbf{B}}{e\eta_e c} - \frac{\nabla p_e}{e\eta_e} \tag{EQ 16}$$

$$\frac{1}{\gamma - 1}\frac{\partial p_e}{\partial t} = -\frac{1}{\gamma - 1}\nabla \cdot (p_e \mathbf{v}_e) - p_e \nabla \cdot \mathbf{v}_e + Q_e \tag{EQ 17}$$

η_e, η_i are the electron and ion resistivities, respectively. Q_e is the electron heat source, and γ is the adiabatic constant.

Jones et al. [9] present an electromagnetic PIC program utilizing massless electrons and including short-range Coulomb collisions. For interspecies collisions, the fluid properties (n, v, T) are interpolated for each species to the mesh and evaluated as a collisional force field when integrating particle motion in a manner that satisfies energy and momentum conservation. For intraspecies collisions, the Langevin equation is used to relax particles toward a Maxwellian distribution. The

collision field increases computational work by 50% and allows the use of large time steps relative to the collision frequency. The electrons are modeled as massless particles with the assumption of quasineutrality:

$$\mathbf{E} = \frac{-\mathbf{J}_e \times \mathbf{B} - \nabla(\rho_e T_e)}{\rho_e} - \frac{m_e}{e}\sum_i \nu_{ei}(\mathbf{v}_e - \mathbf{v}_i) \qquad \text{(EQ 18)}$$

This equation is solved for **E** assuming no displacement current. The equations are subcycled to satisfy the vacuum Courant condition.

In addition to the approximation of a particle species either partially or entirely as a fluid, another method of speeding up electromagnetic simulation is using an implicit solution for the fields. In an explicit electromagnetic solution, the time step is restricted by the Courant condition:

$$\Delta t < \frac{\Delta x}{c} \qquad \text{(EQ 19)}$$

This is often considerably more prohibitive than the stability limitation on time step from the explicit particle push:

$$\Delta t < \frac{2}{\omega_p} \qquad \text{(EQ 20)}$$

While not a fluid method, implicit methods must often be coupled with fluid models to obtain significant speed-up and can also provide increased computational efficiency to particle codes without fluid species.

Brackbill and Forslund [10] developed an implicit discretization of Maxwell's equations for non-relativistic plasma simulation, including an expression for current using the plasma pressure tensor. The stability is limited by the propagation of sound waves instead of electromagnetic waves. High frequency waves (those not resolved by the time step) are damped. The dispersion in the implicit moment equations reduces the finite grid instability. Accuracy and stability are empirically observed when Δt satisfies

$$(O(10^{-1}) < \nu_{th}\Delta t/\Delta x = (\lambda_D/\Delta x)(\omega_p \Delta t)) < O(1) \qquad \text{(EQ 21)}$$

The evolution of a Weibel instability is simulated using a time step $\omega_p \Delta t = 5$. No energy equation is used in this model.

Bowers [11] developed and tested an implicit electromagnetic solver appropriate to the simulation of high frequency, small wavelength plasma systems. An implicit Crank-Nicholson finite differencing of Maxwell's equations is used. High frequency radiation is damped and performance of the field solve is comparable to the standard explicit solve. Only cases with modest Courant numbers retain favorable accuracy, though stability is retained for high Courant numbers. The method was used to compute small wavenumber dispersion relations of bounded plasmas.

Relativistic Monte Carlo Collision Model

Monte Carlo collisions use the cross section to calculate the probability of collision and the scattering angle. The method of calculating collision probability is the same as for non-relativistic

collisions, so the null collision method can be applied. In this section, we consider the scattering angle for relativistic collisions. The doubly differential cross section, Eq. (22), is used to calculate the scattering angle after a collision. We use the singly differential cross section to get the secondary energy after an ionization collision.

The cross section for the relativistic case is difficult to find in the literature. The cross sections for the non-relativistic case often fail for the intermediate and the relativistic regions. Generally the cross sections for the relativistic case do not work well for the other cases. We define the criteria for relativity as $\beta = v/c \geq 1/3$ to distinguish the collision type somewhat arbitrarily; one could choose a different boundary when more precision is needed.

For relativistic elastic collisions, we will use the Wentzel Model [12], which is good for relativistic collisions and also is reasonable for the intermediate regime. The angular distribution function of the Wentzel model is as follows:

$$f(\chi) = \frac{1}{\pi}\frac{A(1+A)}{(2A+1-\cos\chi)^2},$$

$$A = \frac{1}{4}\left(\frac{h}{p}\right)^2 (0.885Z^{-1/3}a_o)^{-2}(1.13+3.76(\alpha Z/\beta)),$$

(EQ 22)

where h is Plank's constant, p is momentum, a_0 is Bohr radius, Z is atomic number, and $\alpha = 1/137$ is the fine-structure constant.

The cumulative distribution for this distribution function gives the scattering angle, χ:

$$\cos\chi = 2A + 1 + \frac{2A(A+1)}{R-A-1}, \qquad \text{(EQ 23)}$$

where $0 \leq R \leq 1$ is a uniformly distributed random number.

Using the basic concept for the relativistic two body kinematics and the scattering angle from Eq. (22) and Eq. (23), the energy after the collision is obtained.

For the elastic collision case, we need the general equation for the differential cross section. After an ionization collision, a secondary electron is created, and its energy must be computed. The secondary electron energy can be obtained from the singly differential cross section.

The calculation method is the same as for the non-relativistic collision. Only the equation for the singly differential cross section is different. The equation for the ionization collision cross section is [13]:

$$\sigma(T,W,I) = \frac{\sigma(T)}{f(T,I)}\left(\frac{1}{(W+I)^2} + \frac{4I}{3(W+I)^3} + \frac{4I}{3(T-W)^3} + \frac{1}{(T-W)^2}\right.$$

$$\left. - \frac{1}{(W+I)(T-W)}\frac{mc^2(2T+mc^2)}{(T+mc^2)^2} + \frac{1}{(T+mc^2)^2}\right) \qquad \text{(EQ 24)}$$

where T is kinetic energy of a incident electron, W is secondary electron energy, I is ionization threshold and $f(T,I)$ is normalizing factor.

We use the cumulative distribution function to get the secondary electron energy in the non-relativistic case.

$$R = \frac{\int_0^W \sigma(T, W, I)\ dW}{\int_0^{\frac{T-1}{2}} \sigma(T, W, I)\ dW} \qquad \text{(EQ 25)}$$

Once we get the secondary electron energy, we can get the energy of two electrons and one positive ion. Using that energy, we made the energy conservation equation.

$$\varepsilon_{scat} + \varepsilon_{ej} + \varepsilon_i = \varepsilon_{inc} + \varepsilon_N - \varepsilon_{ion} \qquad \text{(EQ 26)}$$

where ε_{scat}, ε_{ej}, and ε_{inc} are energies of the scattered, ejected, and incident electrons, respectively. ε_i and ε_N are the energies of the created ion and the target neutral atom, and ε_{ion} is the ionization threshold energy.

Because of the large ion-to-electron mass ratio, we can assume that the momentum of the incident electron is much less than the momentum of the neutral atoms. In other words, the incident electron strips an electron off the neutral, and the neutral becomes an ion, continuing on its trajectory virtually undisturbed. This assumption allows us to rewrite the above energy balance equation as:

$$\varepsilon_{scat} + \varepsilon_{ej} = \varepsilon_{inc} - \varepsilon_{ion} \qquad \text{(EQ 27)}$$

Because we know the ionization threshold energy, incident energy, and ejected energy, we can get the scattered electron energy easily. Once we get the scattered electron energy, we can obtain the scattering angle of the secondary electron in a same way. Obtaining the scattering angle requires the doubly differential cross section as in other collisions. The doubly differential cross section that is used for the relativistic ionization collision is [13]:

$$\sigma(T, W, \chi, I) \propto \left(G_3(T, W, I)^2 + (\cos\chi - G_2(T, W, I))^2\right)^{-1},$$

$$\text{where } G_2(T, W, I) = \sqrt{\frac{(W+I)(T+2mc^2)}{T(W+I+2mc^2)}},$$

$$G_3(T, W, I) = \alpha\sqrt{\frac{I(T-W-I)}{TW}}, \quad \text{and}$$

$$\alpha = 0.6\left(\frac{mc^2}{T+mc^2}\right)^2 \qquad \text{(EQ 28)}$$

Next, using cumulative distribution function, we can get the scattering angle after the ionization collision event:

$$\cos\chi = G_2 + G_3 \tan\left((1-R)\left(R\,\mathrm{atan}\left(\frac{1-G_2}{G_3}\right)\right) - R\,\mathrm{atan}\left(\frac{1+G_2}{G_3}\right)\right) . \quad \text{(EQ 29)}$$

In Phase I, the relativistic collision model was implemented in the 1D OOPD1 code.

Neutral Desorption Model

Partially under the support of Phase I, a model for the surface desorption of neutrals was developed. The main mechanism for desorption due to energetic ion impact appears to be due to electronic sputtering, in which energetic ions deposit energy in a medium, creating a cylinder of energetic atoms and molecules [14,15,16]. The non-radiative energy relaxation processes transport the energy back to the surface of the material, where it leads to the ejection of atoms and molecules when the binding energy is exceeded. Recent molecular dynamics (MD) results have been more successful than so-called "thermal spike" diffusive models for these sub-picosecond phenomena.

Consider ion impact on a medium at an angle θ as measured from the surface normal. The yield at normal incidence, Y_0, must be determined empirically. The angular dependence is obtained from a curve fit based on backscatter data from [17]:

$$\frac{Y(\theta)}{Y_o} = 1 + 1.82\exp(0.09\times\theta). \quad \text{(EQ 30)}$$

The curve fit and data are shown in Fig. 5. The backscatter data appears to correlate well with the electronic sputtering rate, rather than the expected 1/cosθ dependence from energy deposition considerations [15].

The energy dependence of the ejection distribution is given by [15]:

$$f(E) = C_1 \frac{2UE}{E_{exc}(E+U)^3} \quad \text{(EQ 31)}$$

where U is the binding energy, $Eexc$ is the excitation energy, and C_1 is a normalizing constant. The energy distribution of Eq. (31) is shown in Fig. 6. This is implemented in the model by inverting the cumulative distribution function to obtain the relation

$$\frac{E}{U} = \frac{R+R^{1/2}}{1+R}, \quad \text{(EQ 32)}$$

where R is a uniformly distributed random number, $0 < R < 1$.

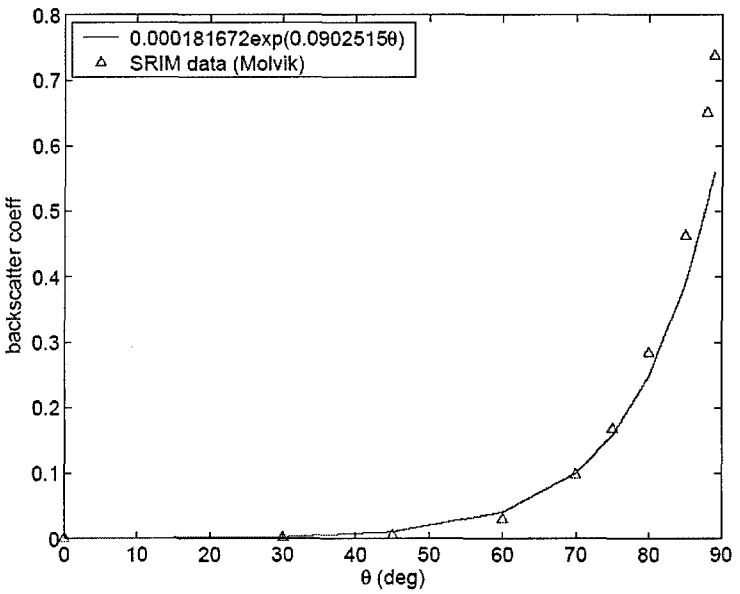

Figure 5. Backscatter coefficient for ion impact based on data from [17].

The angular distribution of the ejected particles is chosen based on the distribution [15]:

$$f(\theta) = C_2 \cos(\theta)^2, \qquad \text{(EQ 33)}$$

where C_2 is a normalizing constant. The angular distribution, which is independent of the incident angle as a consequence of the energy relaxation mechanisms, is shown in Fig. 7. The angle is chosen from this distribution using a Monte Carlo rejection scheme.

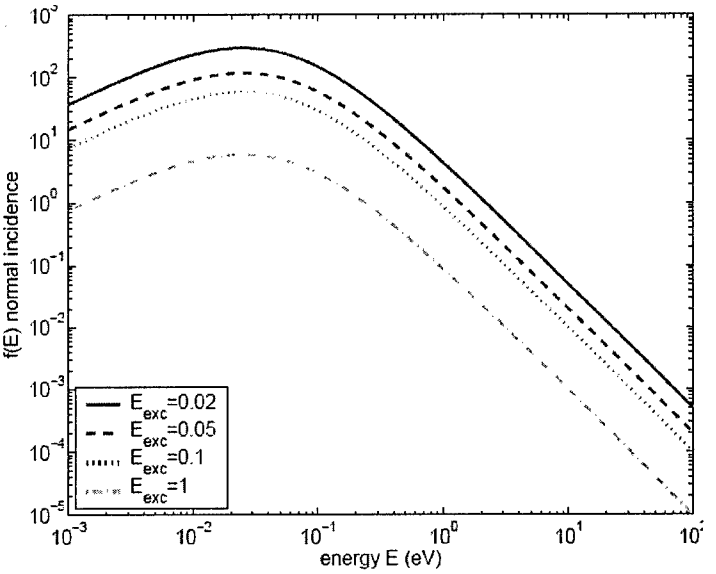

Figure 6. Energy distribution of atoms/molecules for a range of excitation energies.

Task 2: Electron Scattering from Metals/Insulators

In this task, the focus is on development of models for electron scattering from metals and insulators. The XOOPIC code currently incorporates the Vaughan model for secondary electron emission [18,19], which includes both single event backscattering and multiple scattering models. Improvements to the Vaughan model are described as well.

The secondary emission coefficient due to electron impact can be written:

$$\delta(\varepsilon, \theta) = \delta_{\max 0}(1 + k_{s\delta}\theta^2/2\pi)W(w). \qquad \text{(EQ 34)}$$

Here, the incident energy is given by $\mathcal{E}$, the angle with respect to the surface normal is θ, $k_{s\delta}$ is a surface smoothness parameter described below, k is also described below, and $\delta_{\max 0}$ is the peak coefficient at normal incidence at the energy $\mathcal{E}_{\max 0}$. The energy dependence appears implicitly in the right hand side of Eq. (34) through

$$W(w) = \begin{cases} (w\exp(1-w))^k, & w \le 3.6 \\ 1.125/w^{0.35}, & w > 3.6 \end{cases} \qquad \text{(EQ 35)}$$

where the normalized energy, w, is given by:

$$w = \frac{\mathcal{E} - \mathcal{E}_o}{\mathcal{E}_{\max 0}(1 + k_{sw}\theta^2/2\pi)}, \qquad \text{(EQ 36)}$$

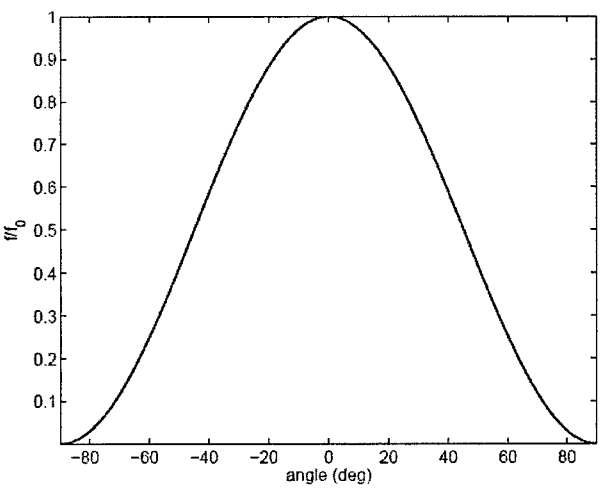

Figure 7. Angular distribution for ejected particles.

where $\mathcal{E}_o$ is the secondary emission threshold, and k_{sw} is a surface-smoothness parameter similar to $k_{s\delta}$. Both $k_{s\delta}$ and k_{sw} vary between 0 for very rough surfaces and 2 for polished surfaces. Typical values are close to 1. The exponent k in Eq. (35) is obtained from a curve fit [19]:

$$k = \begin{cases} 0.56, & w < 1 \\ 0.25, & 1 \le w \le 3.6 \end{cases} . \qquad \text{(EQ 37)}$$

The energy dependence is shown in Fig. 8, and the angular dependence is shown in Fig. 9 for electron generated secondaries. Similar yield relations can be obtained for ion-induced secondaries, sputtering, and desorption.

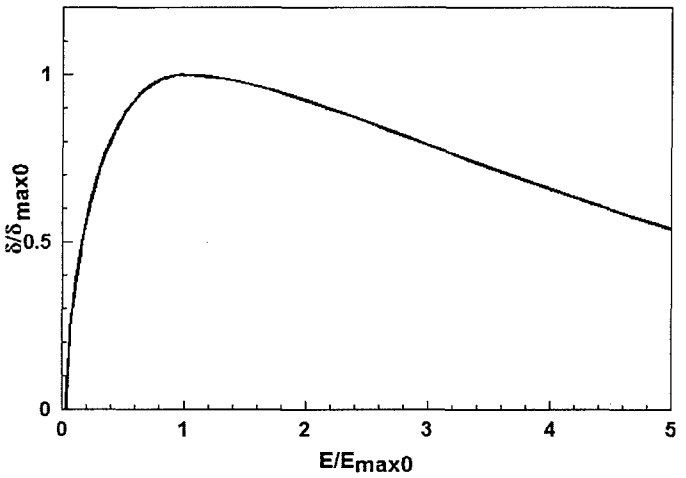

Figure 8. Energy dependence of the secondary emission coefficient.

A schematic of the energy distribution of emitted particles is shown in Fig. 10. Reflected particles typically comprise about 3% of the total particles and are incident electrons reflected at the surface, so they have the full incident energy. Backscattered primaries, comprising about 7% of the ejected electrons, are incident electrons that have penetrated the surface and scattered several times before scattering out of the surface, and consequently they have energy between zero and the incident energy. True secondaries, comprising about 90% of the ejected population, gain sufficient energy to escape the surface by interactions between the incident particle, the free and bound electron populations, and the solid state lattice. The distribution of the true secondaries is taken as a Maxwell-Boltzmann distribution at a temperature *Te* on the order of tens of eV:

$$f(\mathcal{E}) = \frac{\mathcal{E}}{(k_B T_e)^2}\exp\left(-\frac{\mathcal{E}}{k_B T_e}\right), \quad \text{(EQ 38)}$$

where k_B is the Boltzmann constant. The angular distribution is taken to be isotropic:

$$g(\theta) = \frac{1}{2}\cos(\theta), \quad \text{(EQ 39)}$$

with θ the angle from the surface normal. The azimuthal angle is chosen randomly.

In the Vaughan model for secondary emission used in XOOPIC, a step wise value of k is used (0.62 for $w < 1$ or 0.25 for $w > 1$). However, another option provides an energy-dependent value for k [19]:

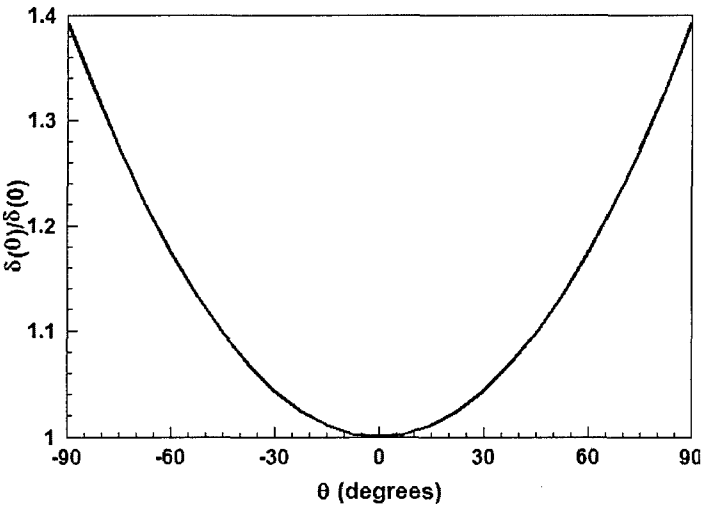

Figure 9. Angular dependence of the secondary emission coefficient.

$$k = \frac{k_1 + k_2}{2} - \frac{k_1 - k_2}{\pi}\operatorname{atan}(\pi \ln w). \quad \text{(EQ 40)}$$

As shown in Fig. 11, when an energy-dependent k is used, based on Eq. (40), the curve fits the experimental data better, especially in the low energy regime $E \leq 250$ eV. In the high energy regime, both models overestimate the secondary yield.

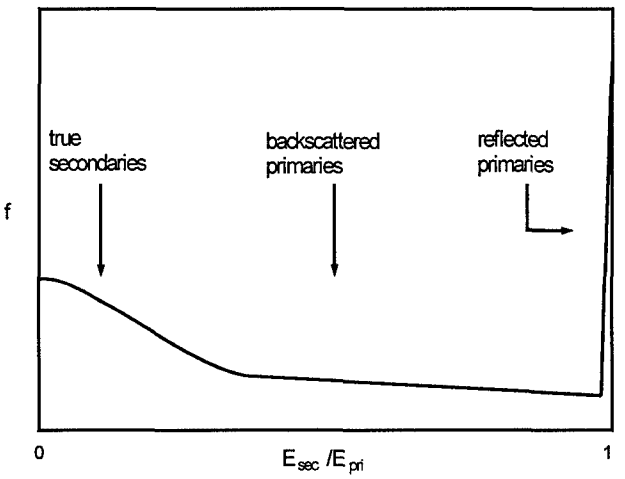

Figure 10. Schematic of the energy distribution of electrons ejected by electron-surface impact.

For the Vaughan model, the secondary electron emission coefficient is small in the relativistic regime, as shown in Fig.12. This is consistent with experimental data in the literature for the MeV range [20].

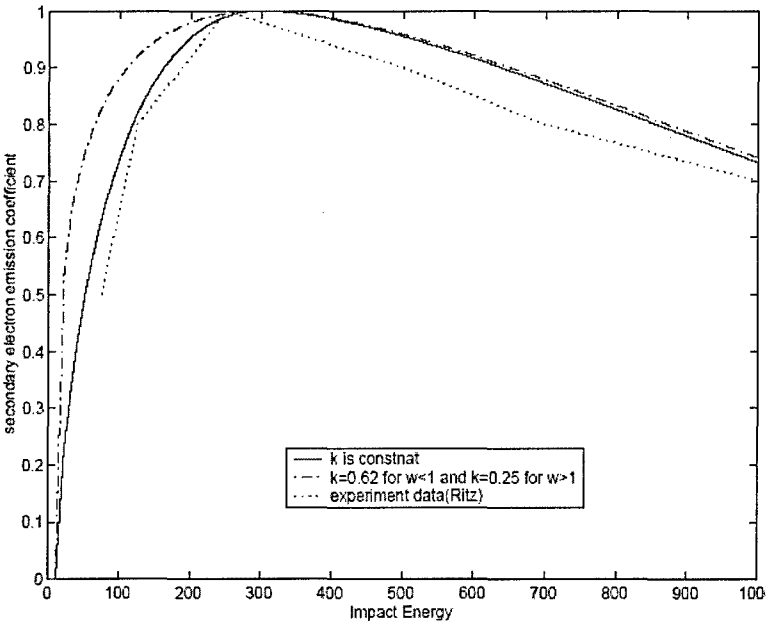

Figure 11. Normalized secondary emission coefficient versus impact energy (eV) for a carbon surface. Experimental data from Ritz [28].

In Phase I of this work, the XOOPIC secondary model has been improved with additional parameterization so that the user can specify the full set of parameters described above from the input file. Furthermore, the model has been further abstracted so that secondary emission is now a property of surfaces. Under the new object model, each surface may have multiple secondary emission properties, one for each specie of incident particle, with independently specified energy and angular dependent yields and emission distribution profiles.

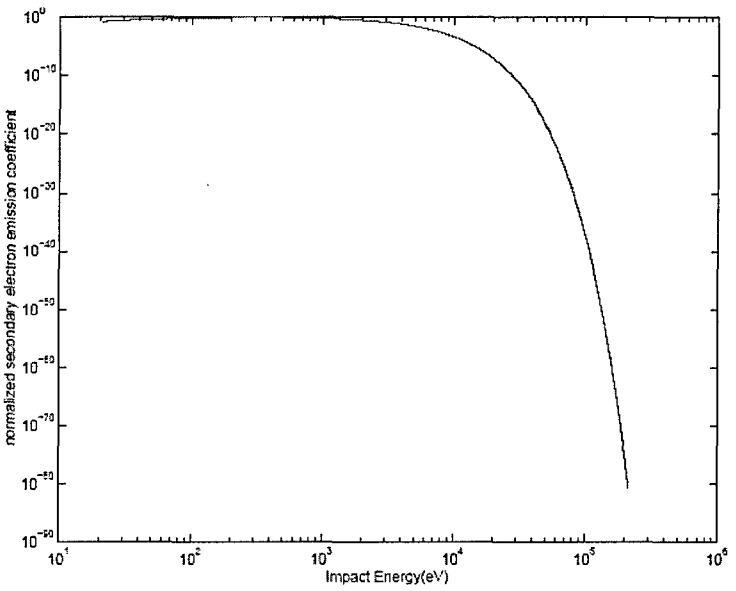

Figure 12. Secondary emission yield in the relativistic regime for the Vaughan model.

In a previous SBIR program (DE-FG03-00ER82964), CCR funded research at N.C. State University to develop and implement an algorithm to accurately and efficiently predict backscatter yield and the trajectories and energies of electrons backscattered by solids [21]. The algorithm considers the energy and direction of an incident electron, the atomic number, atomic mass, and density of the solid, then determines a statistically reasonable path for the electron through the solid via Monte Carlo techniques. This so-called plural scattering model traces the path of an electron through the solid until the electron loses all of its energy or leaves the solid as a backscattered electron. Such a model has been used in a variety of applications, but in this case the interest is predicting the behavior of backscattered electrons. When applied to large numbers of electrons, the program provides statistically accurate results. In particular, excellent agreement is seen between the backscatter coefficients measured by Hunger and Kuchler and those predicted in this program [22], as shown in Figure 13. Furthermore, the angular distribution and energy distributions of backscattered electrons predicted are consistent with those measured by Bishop [23].

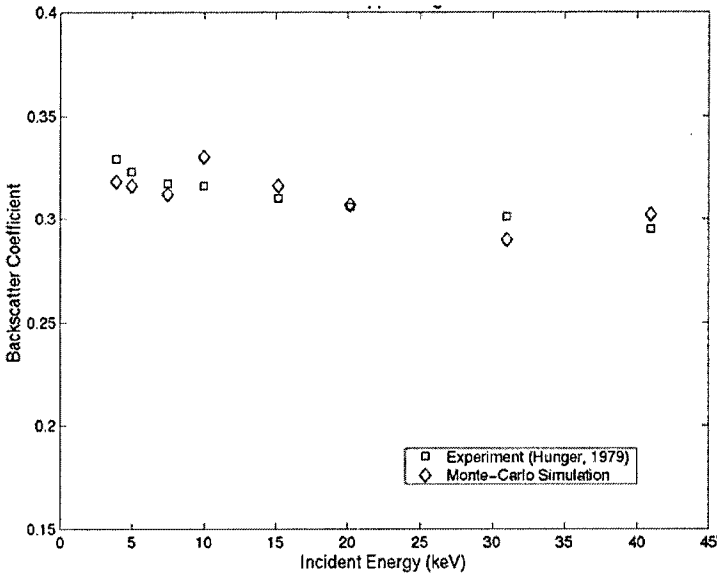

Figure 13. Variation of the backscatter coefficient with incident energy for a copper target. Each predicted value of the backscatter coefficient was determined by modeling 1000 electrons.

In Phase I, the above model was implemented in CCR's Beam Optics Analysis (BOA) finite element code to track backscattered electrons in a collector. Figure 14 shows a 3D conical collector with three generations of secondary electron trajectories. Each generation is plotted in a different color. The spent beam is injected with appropriate initial conditions in an external magnetic field.

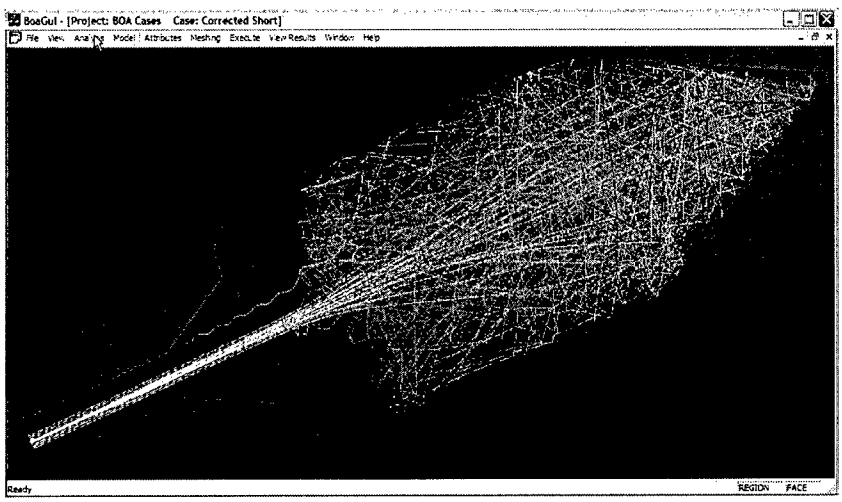

Figure 14. Simulation of a collector with backscattered electron emission. Each color represents one generation of backscattered electrons

With mesh refinement, the mesh density is increased in regions containing electrons and coarsened elsewhere. Fig. 15 shows the final mesh.

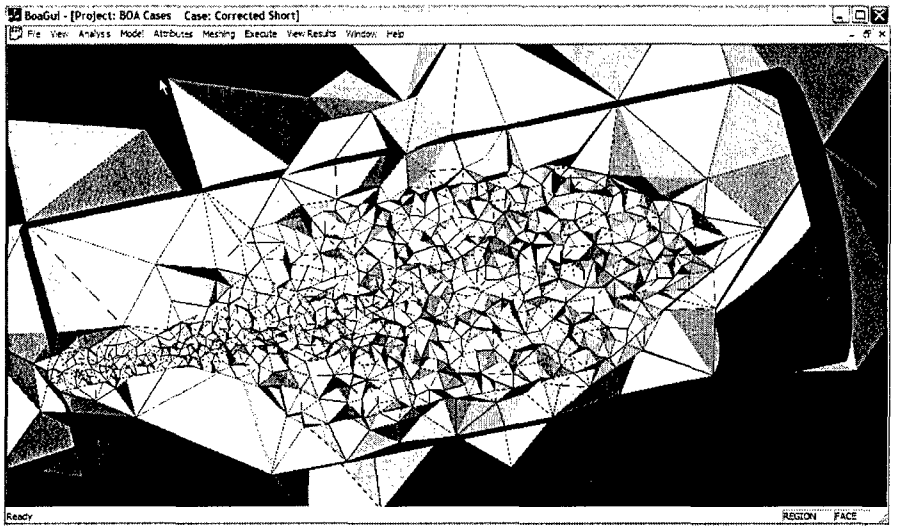

Figure 15. Unstructured, adapted mesh in a collector with backscattered electron emission.

Task 3: High Voltage Breakdown on Insulator Surfaces

Breakdown due to high voltage at insulator surfaces is an important limiting factor in achieving the high fields needed for high power in microwave sources [24]. The effect can be attributed to a number of interesting physical effects. Here we consider the single surface multipactor, possibly initiated by field emission (described in Task 1) and particle-impact induced outgassing (desorption processes described in Task 1).

The XOOPIC code includes the Vaughan secondary model described in Task 2. This model plays a key role in insulator breakdown by single-surface multipactor discharge. Single surface multipactor has been described in the literature [25] and simulated using XOOPIC [26]. In the single surface multipactor (see Fig. 16), electrons in the vicinity of an insulating surface are accelerated in RF fields in the direction tangential to the surface normal, gaining energy. A net positive charge on the surface supplies a DC electric field component, which attracts these electrons toward the surface. The electrons impact the surface in a number of RF cycles determined by the strength of the DC electric field (and hence the surface charge state), the initial energy of ejection for the electron, and the RF frequency. Upon impact with the insulator surface, the electrons may generate secondary electrons, depending on the energy and angle of impact. Ejection of secondary electrons leaves behind an immobile positive charge at the insulator surface, which generates the DC electric field that causes the ejected electron to make an excursion in the direction of the surface normal and eventually return to the surface. When the gain in energy during an excursion due to the RF fields is sufficient to result in impact energies and angles conducive to a secondary emission coefficient greater than unity, the multipactor can grow in time. Saturation ultimately occurs due to effects at the edges of the surface, or due to space charge effects if a plasma is formed at the surface. High density multipactor can result in absorption and reflection of RF power, which can significantly degrade device performance or even damage devices. This effect can occur on either side of the surface.

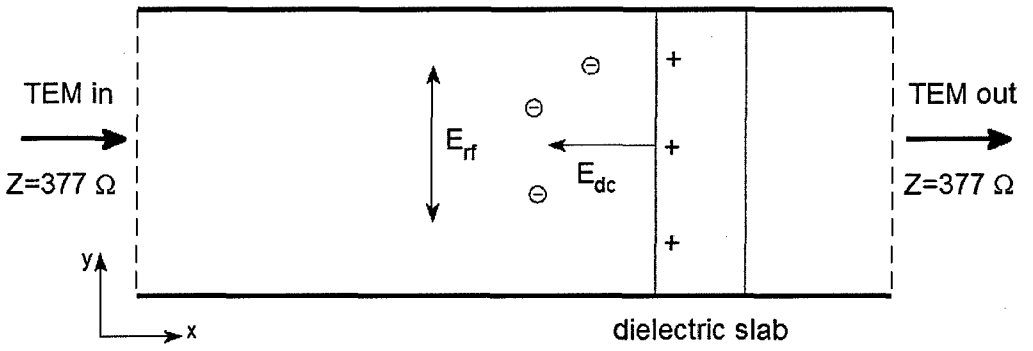

Figure 16. Schematic of insulator breakdown via single surface multipactor.

In Phase I of this work, the field emission model was implemented in OOPD1 as discussed above, the secondary model was implemented, and the Monte Carlo collision model was extended to the relativistic regime as described in Task1 and implemented and tested in OOPD1.

Also, in implementing the collision model in OOPD1 and verifying with XOOPIC, a discrepancy was found in the ion drift velocity for common gases with the same cross sections. To find the drift velocity for He ion in helium gas, PIC/MCC simulations on He ions were performed by using XPDP1 and XOOPIC codes. Two parallel electrodes having the area of 1 m2 are separated by the gap of 1 m. The voltage of 200 V is applied between two electrodes. Initially, the ions with uniform density and zero temperature are distributed randomly on the simulation domain. The ion density is set to be very low so that they themselves do not change the electric field of 200 V/m. The pressure of background helium gas is 1 Torr. The ions gain momentum from the electric field while they lose momentum through collisions with background gas. After several collisions, their macroscopic mean velocity reaches steady state. When the thermal diffusion of ions is ignored, the ion drift velocity is expressed as

$$\boldsymbol{u} = \frac{e}{M\nu_m}\boldsymbol{E}, \qquad \text{(EQ 41)}$$

where M is the ion mass and ν_m is the ion-neutral collision frequency for momentum transfer. In XPDP1 and XOOPIC codes, the elastic and charge exchange collisions for ions are taken into account.

Fig. 17 shows the ion drift velocity obtained from recent XPDP1 and XOOPIC simulations. Since the simulations were performed for identical physical systems, the drift velocities should be the same, but differ by a factor of 8. In the XOOPIC simulations, the steady-state ion drift velocity varied for different ion densities or number of superparticles.

From these indications, we corrected errors in the Monte Carlo source code of XPDP1 and XOOPIC. To validate the modified codes, the theoretical velocity of Eq. (41) was compared with that obtained from XPDP1 and XOOPIC for an analytically tractable model elastic collision cross section that is inversely proportional to the ion velocity (so that the collision frequency is independent of the ion velocity). For simplicity, the charge exchange collision was neglected. The simulation results of XPDP1 and XOOPIC are now in good agreement with the theoretical result, as shown in Fig. 18.

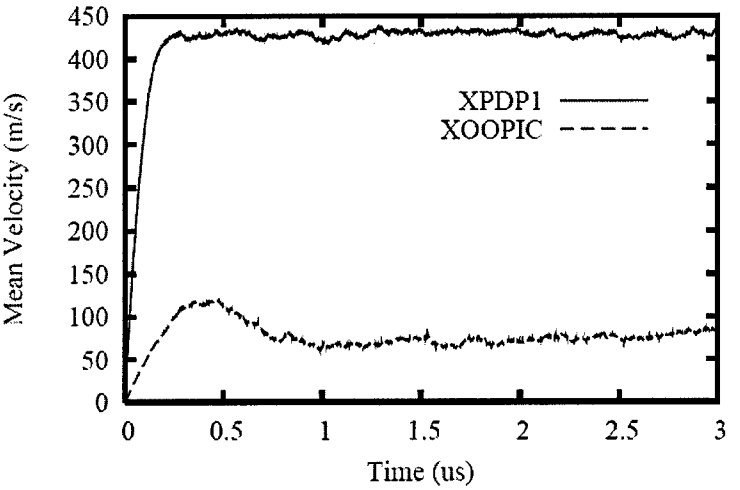

Figure 17. Erroneous result: the drift velocity as a function of time does not agree.

Simulations using experimental cross sections also show good agreement between XPDP1 and XOOPIC simulation results for identical cross section, without dependence on density or numerical particle weight, as shown in Fig. 19.

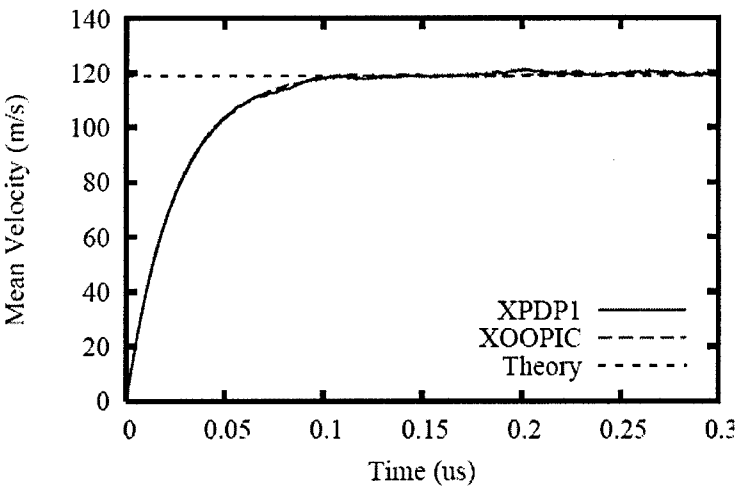

Figure 18. Good agreement for modified XPDP1 and XOOPIC with theoretical result for analytic model cross section with energy-independent collision frequency.

Task 4: Intense Heat Fluxes

In high voltage microwave sources, intense heat fluxes occur when energetic electrons impact surfaces such as collectors, anodes, or beam intercept at unintended locations. Other mechanisms of heat deposition can include plasma bombardment. Although electron flux ideally should be confined to the collector surface, electrons often also impact other surfaces. Beam instabilities can deposit significant fluxes on unintended surfaces, including the anode and the slow wave circuit, resulting in heating that leads to outgassing or even permanent damage. The outgassing can result in plasma formation, which further disrupts the beam and absorbs or reflects microwave power, decreasing device efficiency or disrupting high power operation.

Since the heat flux corresponds to energy deposition by particles, a kinetic method of tracking particles and measuring the energy deposited at surfaces is required. Since sputtering and surface damage are also of interest, it is useful to model the distribution of particle impacts in space, time, energy of impact, and angle of impact.

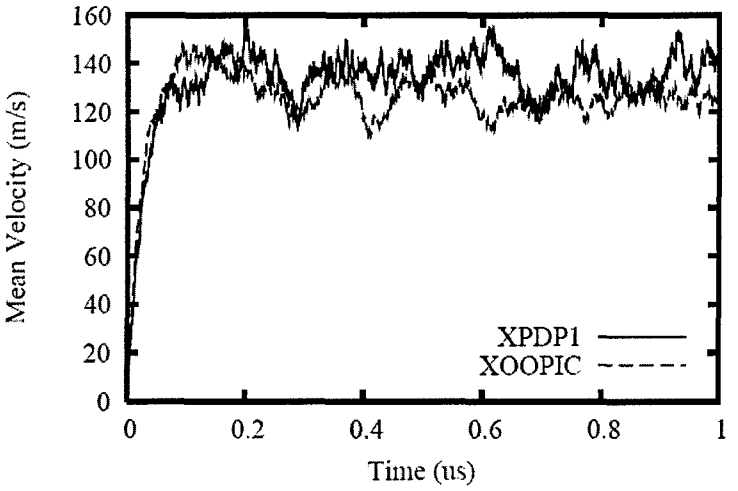

Figure 19. Modified XPDP1 and XOOPIC show good agreement of ion drift velocity for experimental cross sections.

XOOPIC currently includes the capability to measure the energy and angle of impact for a given surface separately, in addition to measuring the current collected on surfaces for each species in the simulation. The existing model is currently limited to simple single element surfaces and provides neither time resolution nor spatial resolution. In particular, the code currently collects the following de-correlated quantities for impacts: $f(x), f(\theta), f(E)$.

In Phase I, a model for obtaining the fully correlated surface flux, $f(x,\theta,E)$, was investigated. The model will allow the user to select some subset of the fully correlated flux distribution for activation on individual surfaces, in order to minimize computation and memory requirements.

The impacting distribution function of particle species is known explicitly in the PIC-MCC methodology. The impacting energy, E, is known from the particle velocity, and the angle from a surface normal, θ is known:

$$\theta \equiv \text{atan}\left(\frac{v_{\perp}}{v_{\parallel}}\right) \qquad \text{(EQ 42)}$$

The particle energy and angle may be weighted to a mesh when impacting boundaries of interest to obtain a gridded representation of the impacting distribution function, $f(E,\theta)$. Fluxes to the surface (energy flux, momentum flux, etc.) may be calculated from the distribution function. The average power absorbed by the surface over time period T is

$$\frac{1}{T}\int_S \int_0^{\pi/2} \int_0^{E_{max}} dE d\theta dS f(E,\theta) \qquad \text{(EQ 43)}$$

The integral $\int dS$ is over surface area. In 1D codes, the integration reduces to a multiplication. For 2D and 3D codes, f is additionally a function of position on the surface and is 4- and 5-dimensional, respectively. An example of a distribution function, f, is shown in Fig. 20.

XOOPIC collects $f(\theta)$ and $f(E)$ independently. This saves memory, as two dimensions of data are stored per boundary (f is a function of position along boundary and E or θ) compared to three

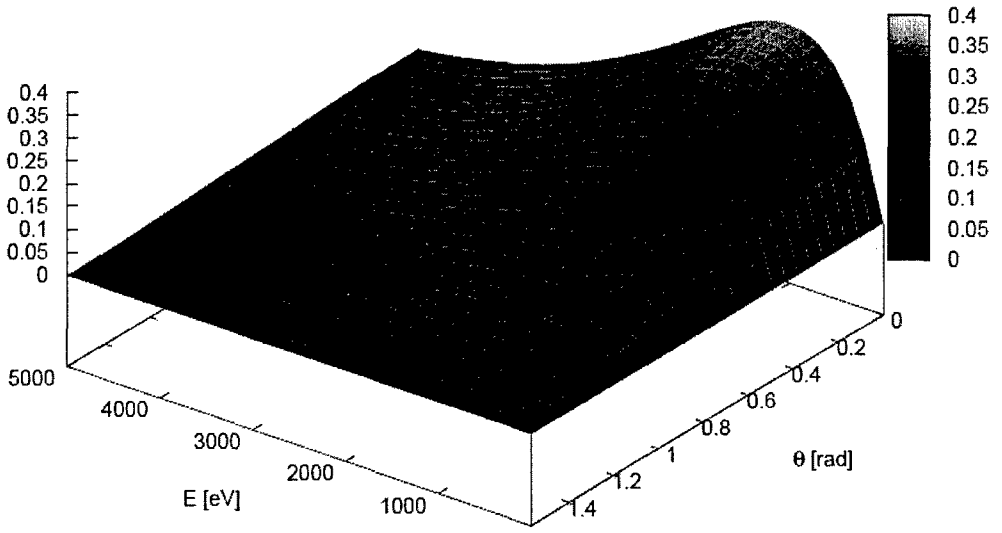

Figure 20. Example distribution function, $f(E,\theta)$.

dimensions for $f(E,\theta)$ and position. However, since $f(\theta)$ and $f(E)$ are uncorrelated, the fluxes (heat flux, momentum flux, etc.) cannot be calculated. Thus it is desirable to obtain $f(E,\theta)$.

The memory needed to store f depends on what information is stored. If the full, time-dependent distribution function is stored in bins ($f(x,t,E,\theta)$), the memory needed to store the data is

$$M = N_T \cdot N_E \cdot N_\theta \cdot \prod_{i}^{d-1} N_{x,i} \qquad \text{(EQ 44)}$$

In this equation, M is the memory used, Nx,i is the number of grid points on the surface in the $\hat{i}$-direction, and d is the number of dimensions in configuration space. N_θ and N_E are the number of bins for angle and energy, respectively, and N_T is the number of time-steps stored. M in Equation (44) must be multiplied by the number of species, though this is usually small. Averaging f over time reduces the system dimension, reduces the needed memory by a factor of N_T, and reduces noise as an affective ensemble average. Another way to reduce the needed memory is to use a functional (spline) representation of f instead of bins, which may be considered zero-order splines. Higher order splines may be used to accumulate a smooth distribution function that has one or more continuous derivatives and conserves one or more moments of the distribution function (number, momentum, energy, etc.). Note that binning f only conserves the lowest moment (number). Using a spline representation of f conserves memory, reduces noise, and provides a convenient way to integrate the distribution function to calculate fluxes. However, the coefficients of the spline must be recalculated as particles hit, which reduces computational efficiency. The trade-offs between computational efficiency and adequate resolution of the distribution function will be studied. The binned data may also be post-processed to reduce noise and obtain a spline representation of f, but higher moments of the distribution function are not conserved.

The use of a single angle, θ, assumes azimuthal symmetry about this angle, which is usually adequate to represent particle interaction with an isotropic surface. An additional angle, Ψ, may be introduced if the full distribution function needs to be calculated. However, this increases computational time and storage requirements, so it should be implemented with an option to enable the full calculation only when required.

Task 5: X-ray Generation and Effects

X-rays cause a number of concerns for high voltage electron devices. First, they pose a safety hazard to personnel and sensitive equipment, requiring shielding and other precautions. X-rays can cause photoemission from various surfaces inside microwave devices, leading to electrons in undesired areas, which can interact with microwaves, background gas, and the electron beam, adversely impacting device performance and possibly even disrupting device operation. The electrons generated by photoemission can also lead to dual surface and single surface multipactors, which can cause significant reflection and absorption of microwave power as well as space charge effects. X-rays can also photoionize background gas and surface impurities, leading to plasma formation, even far from the electron beam. Indeed, cross sections for ionization can be much larger for electrons formed in modest voltage regions than for high voltage beam electrons, so that these photoelectrons can become a more significant source of plasma than the more dense beam.

Energetic charged particles undergoing rapid acceleration, for example in collisions with neutral particles, interaction with strong magnetic fields, or collisions with solid matter, emit electromagnetic radiation in a broad spectrum, including x-radiation. In such problems it is useful to develop the formalism in a way that relates the radiation intensity and polarization directly to properties of the charged particle trajectory and motion. The total radiation emitted, the angular distribution of radiation, and its frequency spectrum are also of interest. For non-relativistic motion the radiation is described by the Larmor result, and for relativistic motion we have more sophisticated theory and calculations [27].

The Larmor power emission for a non-relativistic, accelerated charge is as follows:

$$P = \frac{2}{3}\frac{e^2}{c^3}|\dot{\mathbf{v}}|^2 \qquad \text{(EQ 45)}$$

Larmor's formula Eq. (45) can be converted into a suggestive form to find the appropriate generalization.

$$P = \frac{2}{3}\frac{e^2}{m^2c^3}\left(\frac{d\mathbf{p}}{dt}\cdot\frac{d\mathbf{p}}{dt}\right) \qquad \text{(EQ 46)}$$

where m is the mass of the charged particle, $\mathbf{p}$ its momentum. The Lorentz invariant generalization is

$$P = \frac{2}{3}\frac{e^2}{m^2c^3}\left(\frac{dp_\mu}{d\tau}\frac{dp^\mu}{d\tau}\right) \qquad \text{(EQ 47)}$$

where $d\tau = dt/\gamma$ is the proper time element, and p_μ is the momentum-energy four-vector.

The following is the four-vector scalar product:

(EQ 48)

$$-\frac{dp_\mu}{d\tau}\frac{dp^\mu}{d\tau} = \left(\frac{d\mathbf{p}}{d\tau}\right)^2 - \frac{1}{c^2}\left(\frac{dE}{d\tau}\right)^2 = \left(\frac{d\mathbf{p}}{d\tau}\right)^2 - \beta^2\left(\frac{d\mathbf{p}}{d\tau}\right)^2$$

In linear acceleration, the motion is one-dimensional. From Eq. (48) it is evident that in that case the radiated power is

$$P = \frac{2}{3}\frac{e^2}{m^2c^3}\left(\frac{d\mathbf{p}}{d\tau}\right)^2 \qquad \text{(EQ 49)}$$

The rate of change of momentum is equal to the change in energy of the particle per unit distance. Consequently

$$P = \frac{2}{3}\frac{e^2}{m^2c^3}\left(\frac{dE}{dx}\right)^2 \qquad \text{(EQ 50)}$$

showing that for linear motion the power radiated depends only on the external forces that determine the rate of change of particle energy with distance, not on the actual energy or momentum of the particle.

In circular accelerators like the synchrotron or betatron, circumstances change drastically. In such a situation, the momentum **p** changes rapidly in direction as the particle rotates, but the change in energy per revolution is small. This means that:

$$\left|\frac{d\mathbf{p}}{d\tau}\right| = \gamma\omega|\mathbf{p}| \gg \frac{1}{c}\frac{dE}{d\tau} \qquad \text{(EQ 51)}$$

Then the radiated power Eq. (47) can be written approximately

$$P = \frac{2}{3}\frac{e^2}{m^2c^3}\gamma^2\omega^2|\mathbf{p}|^2 = \frac{2}{3}\frac{e^2c}{\rho^2}\gamma^4\beta^4 \qquad \text{(EQ 52)}$$

where we have used $\omega = c\beta/\rho$, ρ being the orbit radius.

The radial component of Poynting's vector can be written:

$$\mathbf{S}\cdot\mathbf{n} = \frac{e^2}{4\pi c}\left\{\frac{1}{R^2}\left|\frac{\mathbf{n}\times[(\mathbf{n}-\beta)\times\dot{\beta}]}{(1-\beta\cdot\mathbf{n})^3}\right|\right\} \qquad \text{(EQ 53)}$$

In Eq. (53) $\mathbf{S} \cdot \mathbf{n}$ is the energy per unit area per unit time detected at an observation point at time t of radiation by the charge at time $t' = t - R(t')/c$. If we wanted to calculate the energy radiated during a finite period of acceleration, from $t' = T_1$ to $t' = T_2$, we would write

$$E = \int_{t=T_1+[R(T_1)/c]}^{t=T_2+[R(T_2)/c]} [\mathbf{S} \cdot \mathbf{n}]dt = \int_{t'=T_1}^{t'=T_2} (\mathbf{S} \cdot \mathbf{n}) \frac{dt}{dt'} dt' \qquad \text{(EQ 54)}$$

We therefore define the power radiated per unit solid angle to be

$$\frac{dP(t')}{d\Omega} = R^2(\mathbf{S} \cdot \mathbf{n}) \frac{dt}{dt'} = R^2 \mathbf{S} \cdot \mathbf{n}(1 - \beta \cdot \mathbf{n}) \qquad \text{(EQ 55)}$$

If we assume the charge to be accelerated only for a short time during which β and $\dot{\beta}$ are essentially constant in direction and magnitude, and we observe the radiation far enough away from the charge that $\mathbf{n}$ and R change negligibly during the acceleration interval, then Eq. (55) is proportional to the angular distribution of the energy radiated. With Eq. (53) for the Poynting vector, the angular distribution is

$$\frac{dP(t')}{d\Omega} = \frac{e^2}{4\pi c} \frac{|\mathbf{n} \times [(\mathbf{n} - \beta) \times \dot{\beta}]|^2}{(1 - \beta \cdot \mathbf{n})^5} \qquad \text{(EQ 56)}$$

If θ is the angle of observation measured from the common direction of β and $\dot{\beta}$, then Eq. (56) reduces to

$$\frac{dP(t')}{d\Omega} = \frac{e^2 \dot{v}^2}{2\pi c^3} \frac{\sin^2\theta}{(1 - \beta\cos\theta)^5} \qquad \text{(EQ 57)}$$

For small angles, the angular distribution Eq. (57) can be written approximately

$$\frac{dP(t')}{d\Omega} \approx \frac{8}{\pi} \frac{e^2 \dot{v}^2}{c^3} \gamma^8 \frac{(\gamma\theta)^2}{(1 + \gamma^2\theta^2)^5} \qquad \text{(EQ 58)}$$

Another example of angular distribution of radiation is that for a charge in instantaneously circular motion with its acceleration $\dot{\beta}$ perpendicular to its velocity β. We choose a coordinate system such that instantaneously β is in the z direction and $\dot{\beta}$ is in the x direction. With the customary polar angle θ, ϕ defining the direction of observation, as shown in Fig. 21, the general formula Eq. (56) reduces to

$$\frac{dP(t')}{d\Omega} = \frac{e^2}{4\pi c^3} \frac{|\dot{\mathbf{v}}|^2}{(1 - \beta\cos\theta)^3} \left[1 - \frac{\sin^2\theta \cos^2\phi}{\gamma^2(1 - \beta\cos\phi)^2} \right] \qquad \text{(EQ 59)}$$

Using the above equations, we can treat each radiation as a photon with a discrete energy [12]. The radiation is negligible beyond the critical frequency,

$$\omega_{crit} = 3\gamma^3 \frac{c}{r_L}, \qquad \text{(EQ 60)}$$

where r_L is the Larmor radius.

Consider a 1 GeV electron orbiting a 10 T static magnetic field. The relativistic momentum factor is $\gamma = 1952$, and the velocity is effectively the speed of light, c, to six places. The gyroradius is 0.334 m. The power radiated is $P = 6\times 10^{-6}$ W, so the electron would lose 1% of its energy in about 270 ns. The critical frequency is $\omega_{crit}/2\pi = 3.2\times 10^{18}$ Hz, with a corresponding critical wavelength of $\lambda_{crit} = 9.4\times 10^{-11}$ m. In order to resolve the wavelength on the mesh, we would need $\Delta x \leq \lambda/4 = 2.4\times 10^{-11}$ m. For a nominal system length of $L = 3r_L$ in each dimension, the required number of cells in each dimension is 4.2×10^{10}, or 1.7×10^{21} cells in a two dimensional simulation. This exceeds the memory capacity of existing computers. Furthermore, the time step required to satisfy the Courant condition is $\Delta t \leq \Delta x/\sqrt{2}c = 5.7 \times 10^{-20}$ s. The cyclotron period is 7 ns, so one orbit would require 1.2×10^{11} time steps, while running to 1% energy loss would require 4.7×10^{12} time steps. Resolving the critical frequency requires a time step $\Delta t \leq 3.1\times 10^{-19}$ s, which is even more untenable.

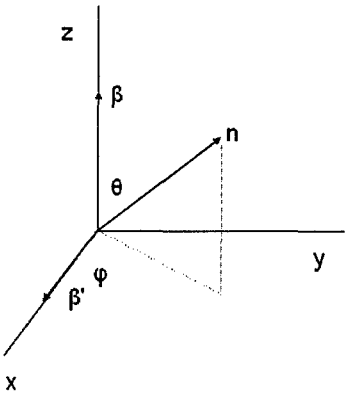

Figure 21. Coordinates for relativistic collision dynamics.

The conclusion of this analysis is that the radiation damping cannot be self-consistently modeled by the standard PIC scheme even for a single particle. Due to the grid resolution and time step constraints, there is no possibility of directly simulating the fields of the radiation emitted over a spectrum sufficient to include a significant fraction of the radiated power.

However, from a previous AFOSR-funded STTR collaboration between U.C. Berkeley and TechXCorp., a model was implemented in XOOPIC to account for the energy lost by particles due to emission of radiation, using an equivalent radiation damping force:

$$F_{rad} = \frac{2}{3}\frac{e^2}{4\pi\varepsilon_o c^4}\frac{\gamma}{\sqrt{\gamma^2-1}}\left(\frac{d\mathbf{p}}{dt}\cdot\frac{d\mathbf{p}}{dt}\right), \qquad \text{(EQ 61)}$$

where **p** is the particle momentum, and

$$\frac{d\mathbf{p}}{dt} = \frac{\sqrt{\gamma^2(t+\Delta t/2)-1}-\sqrt{\gamma^2(t-\Delta t/2)-1}}{\Delta t}mc. \qquad \text{(EQ 62)}$$

This radiation damping term allows for the power loss of accelerating particles, even though it is not possible to track the radiation emitted on these time and space scales.

Task 6: Detailed Structural Visualization

The VLAB code will be based on an extended version of UCB's XOOPIC code. This code is a very flexible and powerful analysis tool for particle simulations, but it is difficult for new and casual users, because it lacks a graphical user interface (GUI).The problem geometry and run time information is specified using a text file of the required format. There are several hundred input parameters documented in forty pages of text. This presents a daunting learning curve for new or casual users. In the Phase II program, we propose to develop a GUI that will simplify the program for the new and casual user while not hindering the advanced user.

The proposed GUI will significantly ease the generation of the data required for XOOPIC. The primary improvement will come from graphical display and input of the problem geometry. The problem parameters will be grouped logically into the categories of Setup, Boundaries, Ports, Emitters and Diagnostics. Advanced features of OOPIC, such as Variables, will be supported and enhanced with user-defined groups. Finally a powerful calculator based diagnostics capability will be added to significantly increase the data analysis capabilities. These features and others will be described in the following sections.

The GUI will be developed using the Qt application development framework. The Qt application program interface (API) is consistent across Windows, Linux, Unix, and Macintosh operating systems, thus enabling a platform independent application deployment. Initial releases of the GUI will target the Windows and Linux environments.

Main Screen

The start up screen will be similar to the one shown in Figure 22. If an input file is selected, a graphical output of the geometry will be displayed in the problem geometry window. During a computation, output of particle positions can be also flagged for display on this screen. The five main menus provide a logical grouping of the many potential parameters controlling the simulation. They are grouped as follows:

- Setup
  - Variables - user defined symbolic variables
  - Grid - dimensions of simulation and grid details
  - Control - time step size, field solver type
  - Species - particle definitions
  - Description - text description of simulation
- Boundaries
  - Conductor - perfect conductor boundaries
  - Equipotential - perfect conductor boundaries that are at a constant potential
  - Dielectric - dielectric boundaries
  - Polarizer - a boundary that allows fractional particle transmission
  - Current - region of current flow
- Ports
  - Exit - a region with minimal reflection of electromagnetic fields
  - Gap - a field excitation boundary
  - Gaussian - a Gaussian profile electromagnetic pulse excitation port

- Emitters
  - Beam - region to generate particles defined by species types
  - Variable weight - spatial variable weight emitter beam emitter
  - Fowler-Nordheim - field emission surface
- Particle Creation
  - Collisions - Monte Carlo collision parameters
  - Load - spatial and Maxwellian velocity distributions of named particle species
  - Plasma source - rectangular region for plasma generation
- Diagnostics
  - Default - list of default diagnostics for display
  - Calculator - user defined operations on analysis variables for display

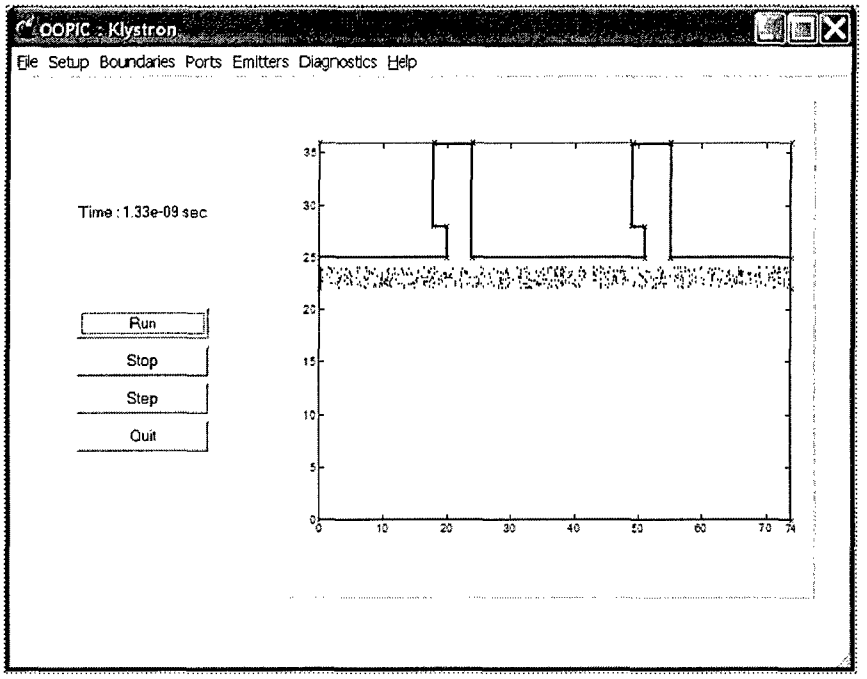

Figure 22. Proposed main screen for OOPIC GUI.

Geometry Entry

In the current version of XOOPIC, the geometry of the simulation is entered as a series of mesh coordinates (or physical coordinates that are mapped to the nearest mesh coordinates). The text entry of these coordinates is very laborious, prone to error, and provides no immediate visual feedback for error checking. In the proposed GUI, the input can be entered using the current method of mesh or physical coordinates along with a new option of entry using cursor position on the mesh display. An example of coordinate entry is shown in Figure 23. Selecting a point on the screen will enter the grid and physical coordinates for the grid point nearest the selected point. If the user enters the grid point by typing in the grid point box, the physical coordinate will be entered automatically in the corresponding box.

In the entry example depicted in Figure 23, the input is for entry of a single, linear, line segment. For generation of more complex geometries, drawing element types such as polyline, arcs, parabolas and circles will be supported. These drawing primitives will allow a user to quickly define the problem boundaries for the majority of simulation types; however, we will also investigate construction of a translator to utilize geometries generated in 2D CAD programs. This translator would allow complex geometries to be drawn using the advanced drawing facilities available in a CAD package familiar to the user. This drawing can then be exported in industry standard formats such as ACIS for import to the proposed XOOPIC GUI. CCR implemented this capability into its

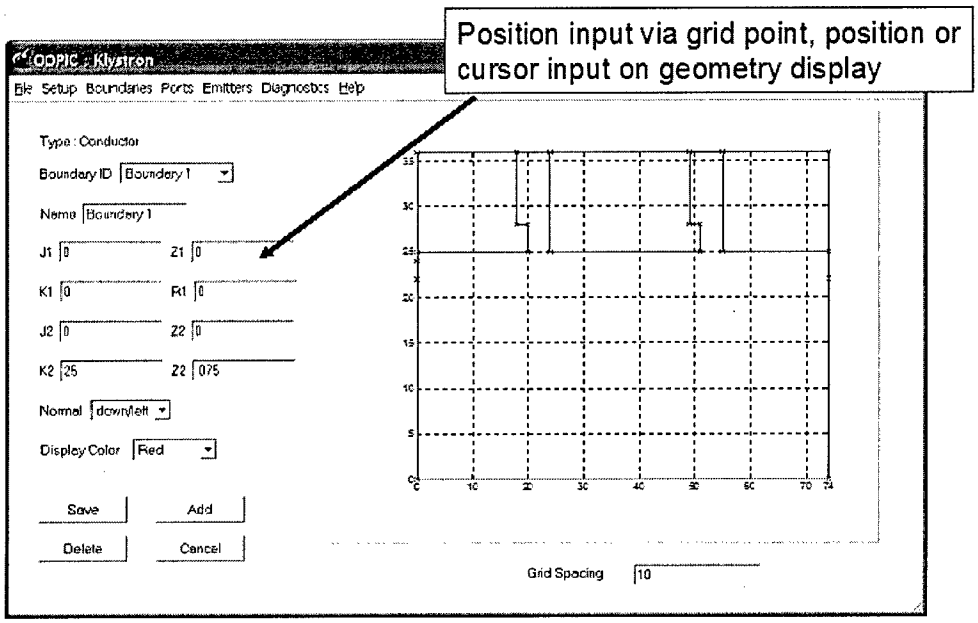

Figure 23. Entry of coordinate information for a new boundary.

current Beam Optics Analysis product. After the CAD drawing is imported by the GUI, the boundary types will be identified for generation of the simulation parameters.

Most boundary types require entry of a only a few parameters to specify the boundary conditions. In addition to boundary specific parameters, however, there are a large number of generic boundary conditions that can be specified but are typically left at their default values or do not apply to the current boundary type. The GUI will separate the required entries from the generic entries using tables selected by tab buttons. In addition, only those generic boundary conditions that are applicable to the current boundary will be displayed. An example boundary dialog screen is shown in Figure 24. This screen also shows how the particle species will be selected from the list of defined types. The species types will be a database of predefined types, such as electrons, and the GUI will allow entry of other user defined types.

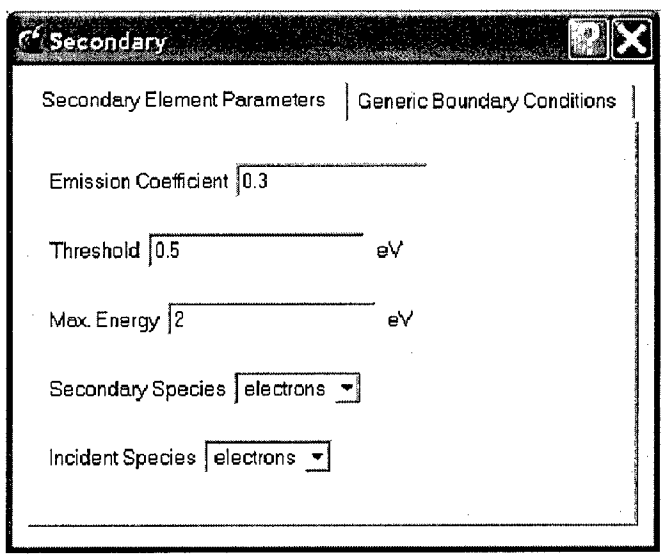

Figure 24. Example dialog box for entry of secondary boundary condition.

Variables

XOOPIC allows user defined symbolic variables. This facility is used to create definitions that can be referenced as input for other simulation parameters. The GUI will support this feature and also allow the variables to be collected in named groups. An example dialog screen showing the *Variable* implementation is shown in Figure 25. In this example, three groups of variables are defined (Constants, Grid Variables and Plasma Variables) that are accessible by selection of the appropriate tab button. The GUI will allow creation, modification, and deletion of each variable group and variables in the group.

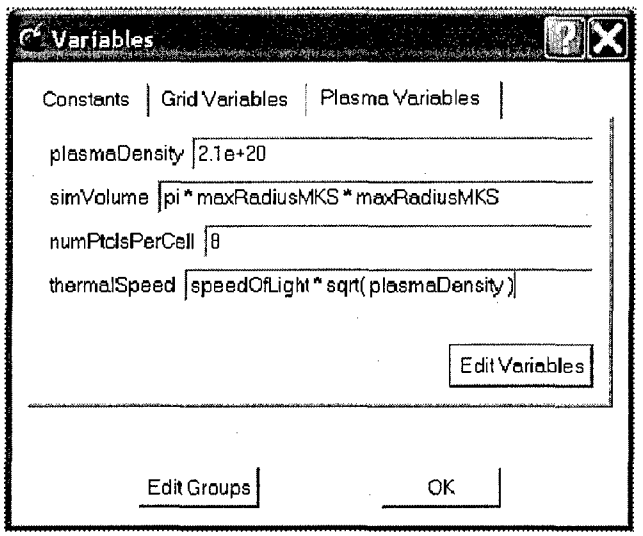

Figure 25. Variable definition dialog box.

Diagnostics

The XOOPIC code graphically displays a large number of default diagnostics that are updated as the simulation progresses. Typical diagnostics include particle position or velocity vs. coordinate, charge density, Poynting calculation, and field quantities. In addition, user defined diagnostics are available. This feature allows generation of time histories of simulation quantities such as the field, Poynting vector and charge density along a line, point or rectangular spatial region. Additional operations that can be performed on analysis data include integration, polarization calculations and power spectral density calculations.

The GUI will retain all the existing diagnostic plotting capabilities of XOOPIC and significantly enhance the user defined diagnostic capability. An arc element will be added to the geometries (line, point, rectangle) that can be used for analysis quantities. The operations that can be performed on these quantities will be greatly increased. A listing of the operations that will be included are:

- General operations: +,-,*,/, absolute value and smoothing,
- Complex operations: Re,Im and conjugate,
- Scaler operations: reciprocal, power, square root, trig operations, derivatives and log,
- Vector operations: dot and cross products, divergence, curl, tangent and normal.

In addition to generating plots, an option to export to file will be added.

Summary

In summary, the Phase I program achieved all the initial objectives and demonstrated feasibility for all tasks.

1. H.A. Schwettman, et al., J. Appl. Phys., 45, 914 (1974).
2. G.N. Fursey, *IEEE Trans. Elec. Insul.* EI-20, 659 (1985).
3. V.I. Rakhovsky, *IEEE Trans. Plas. Sci.* PS-15, 481 (1987).
4. K. L. Cartwright, J. P. Verboncoeur, and C. K. Birdsall, "Nonlinear hybrid Boltzmann–particle-in-cell acceleration algorithm," *Physics of Plasmas* 7, 3252–3264 (2000).
5. T. J. Sommerer and M. J. Kushner, "Numerical investigation of the kinetics and chemistry of rf glow discharge plasmas sustained in He, N2, O2, He/CF4/O2, and SiH4 /NH3 using a Monte Carlo-fluid hybrid model", *Journal of Applied Physics* 71 (1992).
6. A. J. Christlieb, R. Krasny, and J. P. Verboncoeur, "A grid-free treecode field solver for plasma simulations with application to a confined electron column in a penning-malmberg trap", *Computer Physics Communications* 164, 306-310\emph (2004).
7. M. A. Lieberman and A. J. Lichtenberg, *Principles of Plasma Discharges and Materials Processing*, Wiley, New York, (1994).
8. Y. A. Omelchenko, "Kinetic simulations of the formation and stability of the field-reversed configuration", *Physics of Plasmas* 7, 1443–1451 (2000).
9. M. E. Jones, D. S. Lemons, R. J. Mason, V. A. Thomas, and D. Winske, "A grid-based Coulomb collision model for PIC codes", *Journal of Computational Physics* 123, 169–181 (1996).
10. J. U. Brackbill and D. W. Forslund, "An implicit method for electromagnetic plasma simulation in two dimensions", *Journal of Computational Physics* 46, 271–308 (1982).
11. K. J. Bowers, "High Frequency Electron Resonances and Surface Waves in Unmagnetized Bounded Plasmas", Ph.D. thesis, University of California at Berkeley (2001).
12. J. M. Fernandez-Varea, E. Acosta, and J. Sempau, "PENELOPE: A code system for Monte Carlo Simulation of Electron and Photon Transport", Nuclear Energy Agency, 2001.
13. D. Bruhwiler, R. Giacone, J. Verboncoeur, and P. Mardahl, "Particle-in-cell simulations of plasma accelerators and electron-neutral collisions," *Physical Review Special Topics-Accelerators and Beams* 4 (2001).
14. E. M. Bringa and R. E. Johnson, *Nucl. Instr. and Meth. in Phys. Res. B* 143, 513-535 (1998).
15. E. M. Bringa, R. E. Johnson and L. Dutkiewicz, *Nucl. Instr. and Meth. in Phys. Res. B* 152, 267-290 (1999).
16. E. M. Bringa and R. E. Johnson, *Nucl. Instr. and Meth. in Phys. Res. B* 180, 99-104 (2001).
17. A. W. Molvik, M. K. Covo, F. M. Bieniosek, L. Prost, P. A. Seidl, D. Baca, A. Coorey, and A. Sakumi, in press (2004).
18. J. W. Luginsland, T. A. Antonsen, Jr., J. P. Verboncoeur, R. W. Lemke, L. Ludeking, P. M. Mardahl, A. T. Lin, Y. Y. Lau, and J. D. Blahovec, Jr., "Computational Techniques," in *Advances in High Power Microwave Sources and Technologies*, ed. R. J. Barker and E. Schamiloglu, IEEE Press, New York N.Y., 376-437 (2001).

19.J. R. M. Vaughan, "A new formula for secondary emission yield," *IEEE Transactions on Electron Devices* 36, 1963-1966 (1989).

20.R. G. Lye and A. J. Dekker, "Theory of secondary emission," *Physics Review* 107, 977-981 (1957).

21.Dustin F. Kapraun, "Monte Carlo Techniques for Predicting Electron Backscattering," Masters Thesis, North Carolina State University, December 2001.

22.H.H. Hunger and L. Kuchler, "Measurements of the Electron Backscattering Coefficient for Quantitative EPMA in the Energy Range of 4 to 40 keV," *Physica Status Solidi (a)* 56, pp. 45-48, 1979.

23.H.E. Bishop, "Some Electron Backscattering Measurements for Solid Targets," International Symposium on X-ray Optics and X-ray Microanalysis (4th: 1965: Orsay, France) 153-8, 1966.

24.A. A. Neuber, L. Laurent, Y. Y. Lau and H. Krompholz, "Windows and RF Breakdown", in *High-Power Microwave Sources and Technologies*, edited by R. J. Barker and E. Schamiloglu, IEEE Press, New York (2001).

25.R.A. Kishek and Y. Y. Lau, "Multipactor Discharge on a Dielectric," *Phys. Rev. Lett.* 80, 103 (1998).

26.A. Valfells, J. P. Verboncoeur and Y. Y. Lau, "Space charge effects on multipactor on a dielectric," *IEEE Trans. Plasma Sci.* 28, 529-536 (2000).

27.J. D. Jackson, *Classical Electrodynamics*, John Wiley and Sons, Inc., (1998).

28.V. H. Ritz, R. E.Thomas, J. W.Gibson, and J. Klebanoff, "Secondary electron emission characteristics of oxidized beryllium cathodes," *Surface Interact. Anal.* 11, 389-397 (1988).

REPORT DOCUMENTATION PAGE

AFRL-SR-AR-TR-05- 0240

1. AGENCY USE ONLY *(Leave blank)*	2. REPORT DATE	3. REPORT TYPE AND DATES COVERED
		01 Sep 2004 - 31 May 2005 FINAL

4. TITLE AND SUBTITLE
(STTR Phase 1 FY04) User-Safe "Virtual Laboratory" Environment for High Voltage Radiation Soruce Experiments

5. FUNDING NUMBERS
65502F
STTR/TX

6. AUTHOR(S)
Dr Bui

7. PERFORMING ORGANIZATION NAME(S) AND ADDRESS(ES)
CALABAZAS CREEK RESEARC INC
20937 COMER DRIVE
SARATOGA CA 95070-3753

8. PERFORMING ORGANIZATION REPORT NUMBER

9. SPONSORING/MONITORING AGENCY NAME(S) AND ADDRESS(ES)
AFOSR/NE
4015 WILSON BLVD
SUITE 713
ARLINGTON VA 22203

10. SPONSORING/MONITORING AGENCY REPORT NUMBER
FA9550-04-C-0069

11. SUPPLEMENTARY NOTES

12a. DISTRIBUTION AVAILABILITY STATEMENT
DISTRIBUTION STATEMENT A: Unlimited

12b. DISTRIBUTION CODE

13. ABSTRACT *(Maximum 200 words)*

CCR and UCB have achieved the Phase I overall technical objective, which was to demonstrate the feasibility of a computational virtual laboratory for simulating high voltage effects. Models in support of this objective were identified and defined in Phase I, with some components implemented in the one-dimensional object oriented code, and others implemented directly in the 2D code. The 1D code serves as a platform for rapid prototyping of new algorithms. The simplicity of the 1D code ensures that the algorithm or model remains the focus, rather than the mathematical and programming details of multi-dimensional implementation. Modes of the formation of a moving plasma cathode interface, scattering of energetic electrons, high voltage breakdown of insulator surfaces, intense heat fluxes to surfaces, generation of x-rays and an intuitive and user friendly graphical user interface were described and readily for implementation.

14. SUBJECT TERMS			15. NUMBER OF PAGES
			16. PRICE CODE
17. SECURITY CLASSIFICATION OF REPORT	18. SECURITY CLASSIFICATION OF THIS PAGE	19. SECURITY CLASSIFICATION OF ABSTRACT	20. LIMITATION OF ABSTRACT
Unclassified	Unclassified	Unclassified	UL